Oil Shale, 2025, Vol. 42, No. 3, pp. 313–342
doi: https://doi.org/10.3176/oil.2025.3.04

ISSN 0208-189X

NMR response model of pore structure and oil occurrence of Chang 7 shale in Ordos Basin, China

Zhaobing Chen(a,b), Mengyu Liang(c,d), Mingyi Yang(e), Weilei Du(f), Chao Wang(f), Yating Lai(f), Peng Liu(g)*, Ruiliang Guo(a,b)*

(a) School of Earth Sciences and Engineering, Xi'an Shiyou University, Xi'an 710065, China
(b) Shaanxi Key Laboratory of Petroleum Accumulation Geology, Xi'an Shiyou University, Xi'an 710065, China
(c) National Engineering Laboratory for Exploration and Development of Low-Permeability Oil & Gas Fields, Xi'an 710018, China
(d) Exploration and Development Research Institute of PetroChina Changqing Oilfield Company, Xi'an 710018, China
(e) Exploration Division of PetroChina Changqing Oilfield Company, Xi'an 710018, China
(f) No. 2 Gas Production Plant of PetroChina Changqing Oilfield Company, Xi'an 710018, China
(g) College of Safety Science and Engineering, Xi'an University of Science and Technology, Xi'an 710054, China

Received 31 December 2024, accepted 27 June 2025, available online 28 July 2025

Abstract. *This study analyzed 25 Chang 7 shale samples from the Ordos Basin, examining geochemical properties, mineral composition, nitrogen adsorption, mercury injection capillary pressure, and NMR T_2 and T_1–T_2 spectra. The results indicate that the shale primarily contains type II_1 and II_2 kerogen, with mature thermal maturity. Organic-rich shales are enriched in clay and felsic minerals, while organic-lean shales show more dispersed mineral compositions. Nitrogen adsorption classified the shale into four types, with type H2 showing the best properties. The study developed pore size conversion models and clarified the occurrence characteristics of hydrogen nucleus components, providing valuable insights for NMR evaluation of shale reservoirs globally.*

Keywords: *shale oil, NMR, Ordos Basin, pore size conversion models, hydrogen nucleus component identification.*

---

* Corresponding authors, pliu52@hotmail.com, ruiliangguo@xsyu.edu.cn

1. Introduction

With the development of shale oil and gas resources, the reservoir characteristics and hydrocarbon occurrence states of shale reservoirs have gradually become central research topics [1–4]. Nuclear magnetic resonance (NMR) technology, as an efficient method for rock physical characterization, has been widely applied in the study of shale oil and gas reservoirs [5–7]. NMR, through T_2 and T_1–T_2 spectra, enables the direct acquisition of information about reservoir pore structure and hydrocarbon occurrence states [8–10]. Specifically, the NMR T_2 spectrum is capable of characterizing the pore size distribution (PSD) of a reservoir [11, 12]. The T_2 relaxation time is primarily influenced by factors such as pore size, shape, and the interaction between fluid and pore walls [13]. Larger pores exhibit longer T_2 relaxation times, while smaller pores tend to show shorter T_2 times. By analyzing the distribution of T_2 relaxation times, it is possible to effectively reveal the PSD of the reservoir, which is especially crucial for the quantitative analysis of micro- and nano-sized pores.

Regarding the occurrence states of hydrocarbons, shale reservoirs are characterized by complex pore types and fluid occurrence states, in contrast to conventional reservoirs where single fluid types within pores are represented by the T_2 spectrum [13]. This complexity results in signal overlap in the T_2 spectrum, rendering a single T_2 spectrum insufficient to fully capture all hydrogen nucleus relaxation features of shale [14]. Consequently, multi-dimensional NMR techniques, particularly the T_1–T_2 spectrum, offer higher resolution and can effectively differentiate the T_1 and T_2 relaxation time variations between free protons and solid (or semi-solid) protons [15]. Free protons exhibit similar T_1 and T_2 relaxation times, whereas solid protons display shorter T_2 relaxation times and a broader distribution of T_1 relaxation times [16]. Therefore, the T_1–T_2 spectrum provides detailed information about the pore structure and aids in the identification of hydrogen nucleus components in shale reservoirs.

Despite substantial progress in utilizing NMR for characterizing shale pore structures and hydrocarbon occurrence states, several challenges remain. The relationship between T_2 spectra and PSD has been extensively studied; however, the inherent complexity of shale pore structures poses significant challenges in accurately mapping T_2 spectra to pore sizes. T_2 spectra are influenced by factors such as pore heterogeneity, PSD, and surface relaxation properties [17]. While linear conversion models based on spherical or cylindrical pore assumptions [18], as well as power-law models for complex geometries [19], have been proposed, these models remain limited, especially when applied to nanopores or complex pore networks. Furthermore, the conventional assumption of constant pore surface relaxation intensity becomes less applicable as fluid wettability varies with pore size, emphasizing the need for more advanced models [20].

The integration of NMR data with other characterization techniques – such as gas adsorption, mercury injection capillary pressure (MICP), and scanning electron microscopy (SEM) – further complicates T_2-to-pore size conversion [13]. Gas adsorption (CO_2 and N_2) is widely used for micropore and mesopore characterization [21], while MICP is suited for macropore assessment [13, 22]. However, these methods measure different pore characteristics, with gas adsorption focusing on pore size and MICP on pore throat size, complicating their direct correlation with T_2 spectra. SEM, providing high-resolution pore morphology images, is primarily used for qualitative analysis and cannot be directly integrated with NMR for quantitative pore size estimation. The misalignment between T_2 spectra and data from these methods complicates accurate PSD fitting, presenting a major challenge for comprehensive shale reservoir characterization.

Moreover, while T_1–T_2 spectra offer promise for identifying the free, adsorbed, and dissolved hydrocarbon states in shale reservoirs, interpreting these spectra in multicomponent systems remains complex [23]. The T_1–T_2 spectra have the potential to distinguish between different proton environments, offering higher resolution for characterizing the relaxation behaviors of free, adsorbed, and dissolved hydrocarbons. Yet the lack of a clear boundary between adsorbed and free states hinders precise differentiation [14]. Additionally, variations in kerogen type, mineral composition, and pore network across different basins and strata may lead to slight differences in the T_1–T_2 spectral recognition of hydrogen nucleus components.

The Chang 7 (Ch-7) shale, located in the Ordos Basin, is one of the most significant shale oil resources in China, offering promising exploration potential and development value [24]. The reservoir exhibits a complex pore structure, containing micro- and nano-sized pores as well as fractures, which results in substantial heterogeneity in pore characteristics [25]. Due to these complex pore features, the occurrence states and mobility of shale oil vary considerably. In particular, the transformation relationships between free, adsorbed, and dissolved hydrocarbons play a crucial role in influencing development strategies and extraction efficiency. Meanwhile, the exploration and development of shale oil also face challenges, such as complex geological conditions, significant reservoir heterogeneity, and high development costs.

Despite some exploration achievements, gaps remain in the application of NMR for pore structure characterization and hydrogen nucleus component identification in Ch-7 shale oil reservoirs. Currently, the T_2 spectrum pore size conversion models and T_1–T_2 spectrum component identification charts specific to the Ch-7 shale are underdeveloped, lacking standardized methods and models for this region. This limitation poses challenges for precise reservoir characterization.

Therefore, this study aims to develop linear and power-law models for T_2 spectrum pore size conversion and to establish an NMR T_1–T_2 spectrum-based hydrogen nucleus component identification chart for the Ch-7 shale oil reservoir. These efforts are expected to address current limitations and provide effective technical tools for precise characterization of shale oil reservoirs in this region. Moreover, the results of this study will contribute to advancing the application of NMR in other continental shale oil and gas reservoirs and offer valuable reference points for the exploration and development of similar shale oil and gas resources.

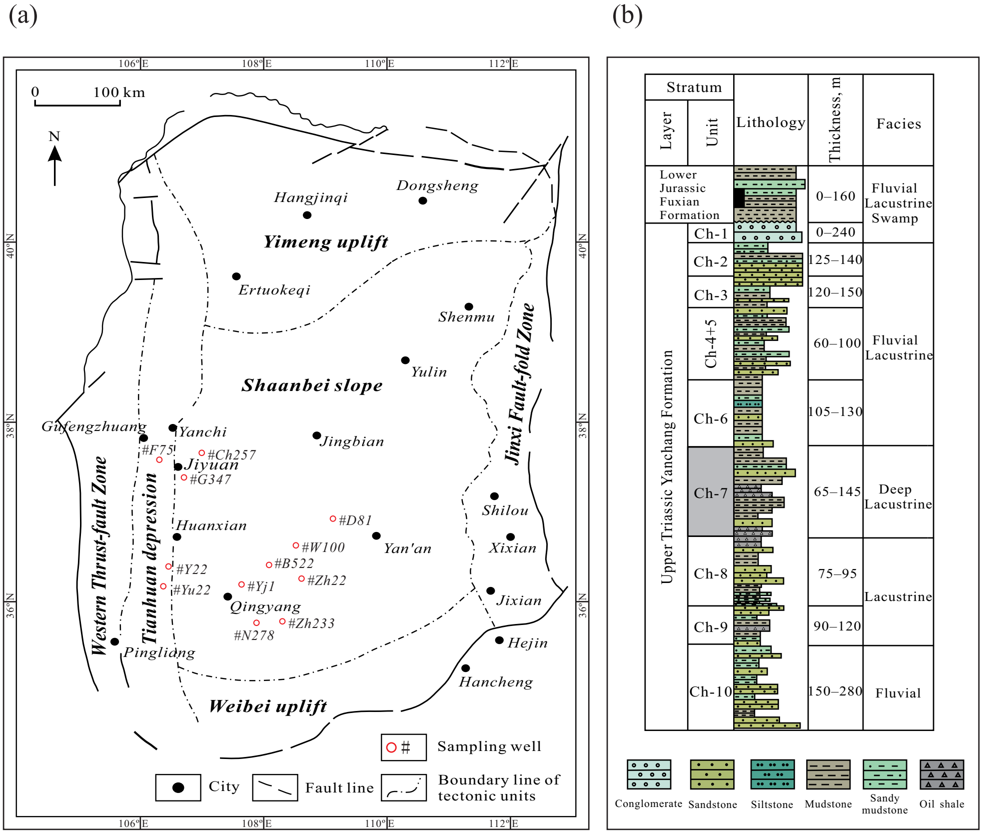

Fig. 1. (a) Structural divisions of the Ordos Basin; (b) stratigraphic column of the Yanchang Formation [26].

2. Geological setting

The Ordos Basin was a lacustrine foreland basin during the Late Triassic [27]. From a tectonic perspective, the basin is divided into six regions: the Jinxi Fault-fold Zone in the east, the Yimeng uplift in the north, the Tianhuan Depression and the Western Thrust-fault Zone in the west, the Shaanbei slope in the center, and the Weibei uplift in the north (Fig. 1a). During the Late Triassic, the basin underwent a transition in sedimentary environment from marine–continental to continental lacustrine. This transition led to the formation of the Yanchang Formation, which is primarily composed of fluvial, lacustrine, and deltaic detrital deposits, including intercalated tuff, mudstone, siltstone, and sandstone [28, 29]. The Yanchang Formation is subdivided into ten sub-members (Chang-10 to Chang-1 from bottom to top) (Fig. 1b).

Ch-7 represents the largest lacustrine sedimentation period, during which widely distributed organic-rich mudrocks were deposited, creating favorable geological conditions for the enrichment of shale oil in the area [24]. The sedimentary thickness of the Ch-7 section ranges from 100 to 120 m, and the average proportions of fine sandstone, sandy mudstone, and organic-rich mudrocks are 21%, 54%, and 25%, respectively (Changqing Oilfield Company). The study area is generally located in the southwestern part of the basin, spanning two secondary tectonic zones. It covers a sedimentary environment ranging from the semi-deep lacustrine slope to the deep lacustrine plain and is presently the main shale oil-producing area in the basin.

3. Samples and methodology

3.1. Samples

Twenty-five lacustrine shale samples, collected from depths ranging between 1622.22 to 2763.90 m across 12 wells, were analyzed for geochemical, mineralogical, and pore structure characteristics using various methods. These samples represent shale deposits from semi-deep to deep lacustrine facies, mainly distributed in the central to southwestern part of the basin, and provide a good representation of the overall characteristics of the Ch-7 shale. The lithology consists primarily of gray-black to black layered or laminated shale, with samples selected based on total organic carbon (TOC), mineral composition, and lithofacies type.

To ensure data comparability and establish a conversion model for the NMR T_2 spectrum to PSD, all experiments were conducted on a single cylindrical plug. The steps were as follows (Fig. 2): samples were cut into 8 cm cylindrical plugs using diamond wire cutting. Non-parallel ends were trimmed and crushed to 200 mesh for TOC, Rock-Eval pyrolysis, and X-Ray

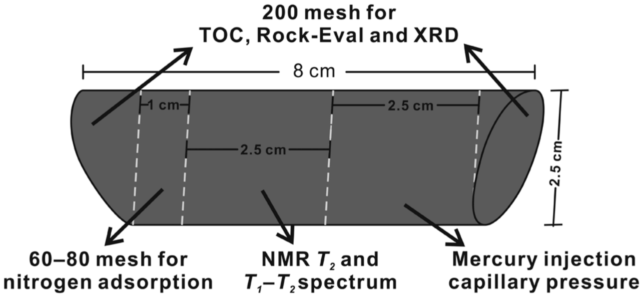

Fig. 2. Schematic diagram of cylindrical plugs dimensions and analytical methods.

diffraction (XRD) analysis. The remaining plugs were then cut into sub-plugs of 1 cm, 2.5 cm, and 2.5 cm for nitrogen adsorption (NA), NMR, and MICP analysis, respectively.

3.2. Methods

The 200-mesh powdered samples were first treated with hydrochloric acid (HCl) to remove inorganic carbonates, followed by rinsing with distilled water until neutral. The samples were then dried in an oven at 60 °C for at least 24 h before the TOC was measured using a LECO carbon/sulfur analyzer (LECO Corporation, USA). The pretreated powders were subsequently subjected to pyrolysis using a Rock-Eval 6 instrument (Vinci Technologies, France) to determine free oil (S_1), residual hydrocarbon generation potential (S_2), and maximum pyrolysis temperature (T_{max}). Mineral composition was analyzed using a Bruker D8 Advance X-ray diffractometer equipped with a Cu tube (Bruker, Germany). Experimental conditions were as follows: scan range of 0 to 140°, scan rate of 2°/min, step size of 0.02°, current ≤40 mA, and tube voltage ≤40 kV.

NA measurements were conducted using an ASAP 2020 adsorption instrument (Micromeritics Instrument Corp., USA). The sample consisted of 0.5 g of 60–80 mesh de-oiled and dehydrated powder. Pretreatment involved incubation at 150 °C for 12 h. NA was carried out at 77.35 K with a differential pressure (P/P_0) ranging from 0.002 to 0.995. The Barrett–Joyner–Halenda (BJH) model and Brunauer–Emmett–Teller (BET) model were applied to gain pore volume (PV), PSD, and specific surface area (SSA).

MICP analyses were performed in accordance with the SY/T 5346-2005 standard, using an AutoPore IV 9500 porosimeter (Micromeritics Instrument Corp., USA). Tests were conducted under controlled environmental conditions at 16 °C, 50% humidity, and atmospheric pressure. Mercury intrusion and extrusion curves were generated over a pressure range of 0.02 to 182 MPa, corresponding to pore radii ranging from 36.75 μm to 4.04 nm.

NMR tests were conducted using a MicroMR12-040V nuclear magnetic resonance analyzer (NIUMAG, China), with a magnetic field strength of 0.3 ± 0.05 T and a main frequency of 12 MHz. To compare the T_2 and T_1–T_2 spectra of shale in different states and characterize hydrogen components in various regions, samples in their original, dry, oil-saturated, and water-saturated states were tested for both T_2 and T_1–T_2 spectra measurements. The test parameters included a waiting time of 2500 ms, echo number of 12,000, scan number of 32, and echo time of 0.15 ms. *n*-Dodecane (C_{12}) was used as a probe reagent to characterize the shale pore structure. Solid hydrogen components (e.g., kerogen) were corrected by subtracting the T_2 spectrum of the de-oiled and dehydrated state from the C_{12}-saturated T_2 spectrum, allowing for accurate determination of shale pore fluid T_2 relaxation times. The drying procedure involved Soxhlet extraction using a dichloromethane–acetone mixture (3:1 volume ratio) for 72 h at 90 °C and 0.3 MPa, followed by vacuum drying at 110 °C for 24 h. For C_{12} saturation, the samples were subjected to vacuum pumping for 24 h, pressurization to 10 MPa, and C_{12}-saturation for 24 h. For water saturation, the samples were immersed in deionized water, vacuum-pumped for 24 h, then pressurized to 10 MPa, and maintained for 24 h.

In this study, micropores, mesopores, and macropores are classified using 100 nm and 1000 nm as diameter thresholds, consistent with previous studies characterizing the PSD of Ch-7 shale and other shale oil plays in China [25, 30, 31].

4. Results and discussion

4.1. Compositional characteristics

The TOC of Ch-7 shale ranges from 0.53% to 22.20%, with an average of 6.05%. T_{max} ranges from 440 to 477 °C, averaging 449 °C. The S_1 and S_2 values range from 0.16 to 7.28 mg/g rock and from 0.47 to 91.66 mg/g rock, averaging 1.99 and 17.19 mg/g rock, respectively. The HI varies from 59 to 413 mg/g TOC, averaging 226 mg/g TOC (Table 1).

Based on the HI–T_{max} intersection diagram, the kerogen in Ch-7 shale is mainly type II_1 to II_2, and is thermally mature (Fig. 3) [32]. Samples OC-10 and OC-7 to OC-9 have reached overmature and postmature stages, respectively.

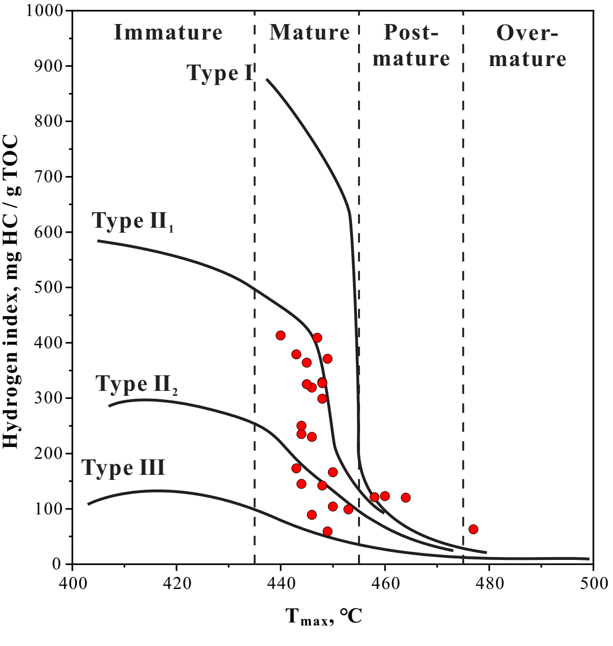

Fig. 3. Relationship between hydrogen index and T_{max}.

Table 1. Geochemical parameters of Chang 7 shale samples

Sample No.	Well	Depth, m	TOC, %	T_{max}, °C	S_1, mg/g rock	S_2, mg/g rock	HI, mg/g TOC
OC-1	Yj1	2058.00	7.29	444	2.45	17.10	235
OC-2	Yj1	2069.00	3.95	450	1.14	6.57	166
OC-3	Yu22	2651.00	12.70	446	2.50	40.55	319
OC-4	Yu22	2666.70	9.86	448	1.58	32.42	329
OC-5	D81	1654.00	3.24	444	0.45	8.10	250
OC-6	D81	1655.12	3.70	448	0.53	11.05	299
OC-7	Zh22	1624.00	6.80	460	2.78	8.36	123
OC-8	Zh22	1630.10	6.17	458	2.43	7.47	121
OC-9	Zh22	1640.70	7.35	464	2.44	8.83	120
OC-10	Zh22	1653.10	1.02	477	0.23	0.64	63
OC-11	W100	2010.40	13.60	449	2.34	50.40	371
OC-12	W100	2014.10	6.07	448	2.06	19.82	327
OC-13	W100	2018.52	4.87	447	2.08	19.91	409
OC-14	F75	2755.47	2.24	443	1.51	3.88	173
OC-15	F75	2756.25	1.78	448	1.28	2.53	142
OC-16	F75	2763.90	8.00	445	3.61	29.09	364
OC-17	Y22	2642.18	6.07	445	3.28	19.71	325
OC-18	Y22	2642.92	0.79	449	0.16	0.47	59
OC-19	Y22	2666.23	0.89	446	0.22	0.79	89
OC-20	B522	1931.50	3.52	453	1.58	3.47	99
OC-21	B522	1947.75	9.07	444	3.33	13.11	145
OC-22	N278	1622.22	7.38	443	3.42	27.95	379
OC-23	Zh233	1802.70	22.20	440	7.28	91.66	413
OC-24	G347	2421.51	2.28	446	0.80	5.24	230
OC-25	Ch257	2521.80	0.53	450	0.17	0.55	104

The mineral composition of all samples is chiefly composed of clays (15.2–66.5%, avg. 50.1%) and quartz (17.0–38.9%, avg. 26.4%), followed by feldspar (3.8–32.9%, avg. 12.2%), pyrite (0–36.1%, avg. 5.9%), and carbonates (0–20.8%, avg. 4.0%). Illite (avg. 21.7%) is the dominant clay mineral, followed by illite/smectite mixed layers (15.7%), chlorite (7.2%), and kaolinite (5.6%) (Table 2). Based on the lithofacies classification map (Fig. 4) [33], the shale samples are mainly composed of argillaceous shale, with minor occurrences of felsic and mixed-type shale. According to TOC, shale samples are categorized into organic-lean, organic-bearing, and organic-rich groups based on the boundary values of 2% and 6% [25, 34]. Organic-bearing and organic-rich shales are typically enriched in clay and felsic minerals, while organic-lean shales are relatively dispersed in mineral composition.

Table 2. Mineral compositions (%) of Chang 7 shale samples

Sample No.	Quartz	Feldspar	Carbonates	Pyrite	Total clays	Illite/smectite mixed layer	Illite	Kaolinite	Chlorite
OC-1	27.6	6.7	1.7	9.2	54.8	16.1	26.0	4.1	8.6
OC-2	22.9	13.8	12.1	4.0	46.9	15.3	23.2	2.9	5.5
OC-3	20.4	8	1.0	8.0	60.9	19.2	37.4	2.1	2.3
OC-4	24.1	10.6	0.5	4.1	59.5	19.2	28.0	7.5	4.8
OC-5	32.9	10.5	2.5	0.7	53.4	14.7	8.9	12.4	17.4
OC-6	20.3	15.6	0.4	0.6	63.1	19.6	11.5	16.8	15.2
OC-7	21.7	10.5	2.1	2.9	59.1	16.7	32.8	1.5	8.1
OC-8	17	8.6	2.2	1.4	66.0	18.4	43.1	1.5	3.0
OC-9	18	7.7	3.7	2.5	65.8	21.7	39.2	1.8	3.1
OC-10	33.6	14.2	1.1	1.0	48.6	14.1	25.9	3.2	5.4
OC-11	18.7	12.8	0.0	23.0	45.5	12.2	20.3	5.7	7.3
OC-12	38.9	13.3	1.1	4.2	40.7	16.8	13.9	3.4	6.7
OC-13	35.3	15.2	1.6	1.0	46.9	12.6	15.6	5.3	13.5
OC-14	29.6	10.1	4.4	1.2	47.5	18.1	10.9	14.7	3.8
OC-15	29.2	9.4	1.4	1.2	54.0	22.2	15.6	12.3	4.0

Table 2. (continued)

Sample No.	Quartz	Feldspar	Carbonates	Pyrite	Total clays	Illite/smectite mixed layer	Illite	Kaolinite	Chlorite
OC-16	24.4	4.4	1.8	2.9	66.5	18.4	30.1	9.7	8.3
OC-17	36.3	12	7.2	1.9	42.6	10.7	14.7	6.5	10.7
OC-18	29.2	3.8	20.8	1.1	42.1	7.2	24.2	3.4	7.4
OC-19	30.4	4.9	15.2	1.1	48.4	40.5	7.0	0.4	0.5
OC-20	20.3	11.7	4.1	4.1	58.9	12.0	41.2	1.7	4.0
OC-21	17.7	15	2.8	27.0	37.5	9.0	24.9	1.3	2.3
OC-22	24.6	9.3	2.5	7.0	56.6	12.1	28.0	4.5	12.0
OC-23	31.3	11.8	2.5	36.1	15.2	4.8	8.7	0.6	1.2
OC-24	28.1	32.6	3.2	0.0	36.1	8.7	6.9	7.4	13.0
OC-25	26.7	32.9	3.3	0.5	36.6	11.9	4.8	8.1	11.9

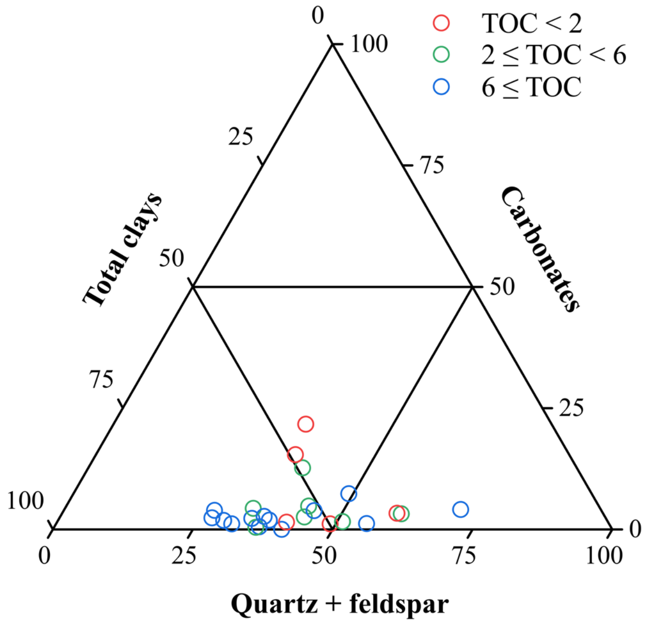

Fig. 4. Mineral and TOC composition classification of Chang 7 shale samples.

4.2. Pore structure of shale based on different methods

4.2.1. Nitrogen adsorption

The adsorption–desorption isotherms of the Ch-7 shale samples generally exhibit a reverse S-shape, with hysteresis loops appearing between the adsorption and desorption curves in the medium to high relative pressure stages (P/P_0 between 0.4 and 0.8) [26]. These hysteresis loops reflect the primary pore structure characteristics of the shale samples. According to the IUPAC hysteresis loop classification [35, 36], four types of loops were identified among the Ch-7 shale samples: H2 type, H2–H3 mixed type, H3 type, and H4 type.

- H2 type is characterized by a relatively wide, vertically oriented hysteresis loop (Fig. 5a). When P/P_0 exceeds 0.5, the desorption curve decreases slowly, forming a desorption plateau. At a P/P_0 of approximately 0.5, the desorption curve drops sharply, forming a distinct loop. This pattern reflects an ink-bottle-shaped pore structure, observed in six samples. The corresponding PSD is primarily concentrated in the micropore range, with a clear peak below 5 nm (around 3 nm) (Fig. 6a).
- H3 type features a narrower hysteresis loop (Fig. 5c). In the high-pressure stage (P/P_0 between 0.8 and 1), the adsorption volume increases sharply, and the adsorption curve approaches verticality. Capillary condensation occurs before the adsorption reaches saturation. The desorption curve runs nearly parallel to the adsorption curve when P/P_0 exceeds 0.5, and a small hysteresis loop forms without a distinct turning point. This reflects a plate-like pore structure, seen in 11 samples. The PSD shows a balanced development of micropores and mesopores, with limited pore development below 5 nm (Fig. 6c).
- H4 type shows a generally smaller hysteresis loop but stronger heterogeneity (Fig. 5d). The adsorption and desorption curves are nearly parallel, indicating a slit-like or inclined plate-like pore structure. This type appears in three samples. The PSD is dominated by micropores and mesopores, with most pores being smaller than 5 nm (Fig. 6d).
- H2–H3 mixed type combines characteristics of both H2 and H3 types, indicating the co-development of ink-bottle-shaped and plate-like pores (Fig. 5b). This type is observed in five samples, and the PSD is similar to that of the H3 type (Fig. 6b).

The PVs of all samples range from 0.0028 to 0.0156 cm^3/g, with an average of 0.0071 cm^3/g. The SSAs range from 0.5859 to 10.0338 m^2/g, averaging 2.5970 m^2/g. The APDs reach up to 14.85 nm, with micropores and mesopores accounting for 76.70% and 23.30% of the total PV, respectively. Among the four pore structure types, PVs follow the order H2 > H4 > H3 > H2–H3 mixed type (0.0079, 0.0071, 0.0070, and 0.0068 cm^3/g, respectively), while SSAs follow the order H4 > H2 > H3 > H2–H3 mixed type (4.6140, 2.7776, 2.5649, and 2.4342 m^2/g, respectively). APDs follow the order H2–H3 mixed type > H3 > H2 > H4 (14.85, 14.40, 14.40, and 10.79 nm, respectively).

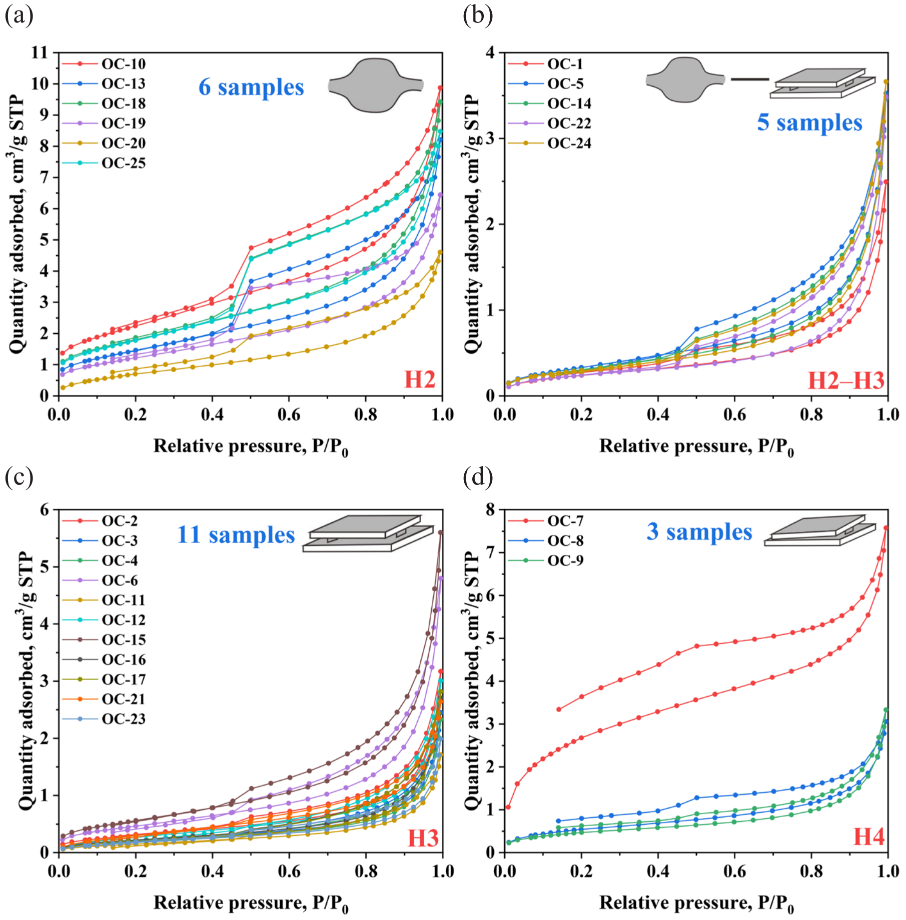

Fig. 5. N_2 isotherms of different hysteresis loop types of Chang 7 shale.

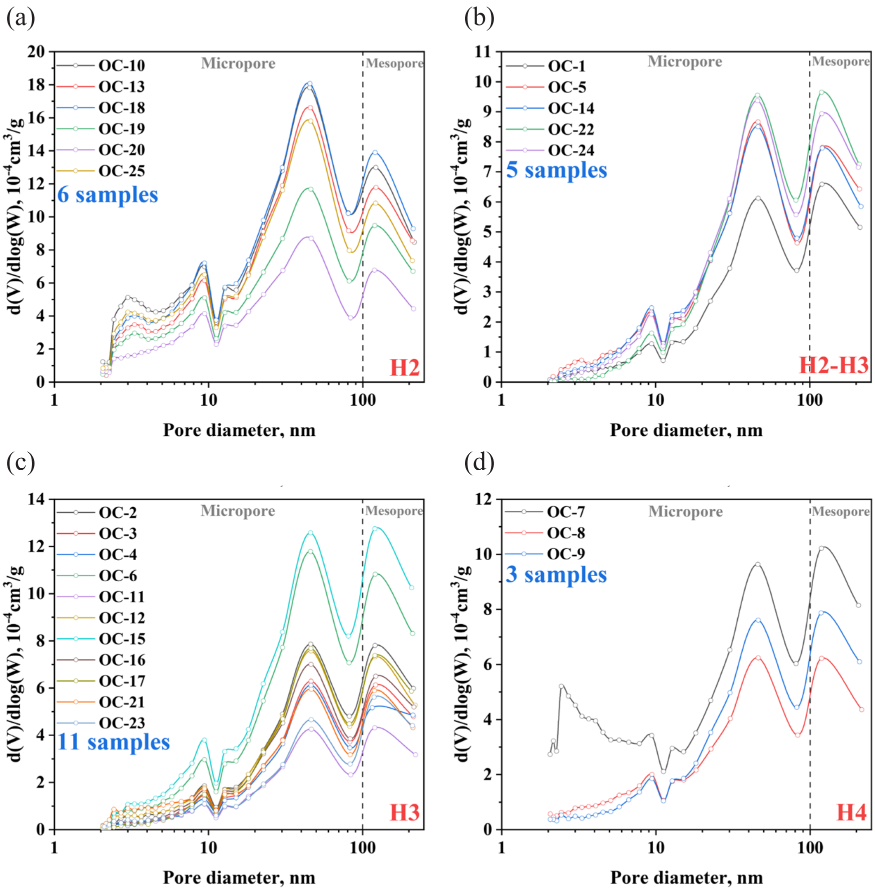

Fig. 6. Pore size distribution of different types of Chang 7 shale based on N_2 adsorption.

4.2.2. MICP

MICP is an effective method for detecting connected pores in reservoirs [13]. The mercury intrusion curves (MIC) can effectively reflect differences in pore structure. Based on MIC morphological variations and established classification criteria from prior studies, the 25 Ch-7 shale samples can be classified into four types:

- Type I MICs are convex upward with a single distinct inflection point (Fig. 7a). The mercury intrusion volume increases rapidly after the inflection point as intrusion pressure rises. The distance between the intrusion and extrusion curves is relatively large. This type includes two samples, with the PSD primarily consisting of micropores, while mesopores and macropores show no significant peaks (Fig. 8a).

- Type II MICs typically exhibit two inflection points, with a concave curve at lower intrusion pressures (Fig. 7c). The distance between the intrusion and extrusion curves decreases. This type includes ten samples, with the PSD dominated by micropores and mesopores, showing a peak at approximately 1000 nm (Fig. 8c).
- Type III MICs show a further reduction in the distance between the intrusion and extrusion curves (Fig. 7d). The intrusion curve is generally flatter. This type includes eight samples, with the PSD mainly consisting of micropores and macropores, and a peak between 1000–10000 nm (Fig. 8d).
- Types I–II include five samples, with well-developed PSDs across micropores, mesopores, and macropores (Figs 7b and 8b).

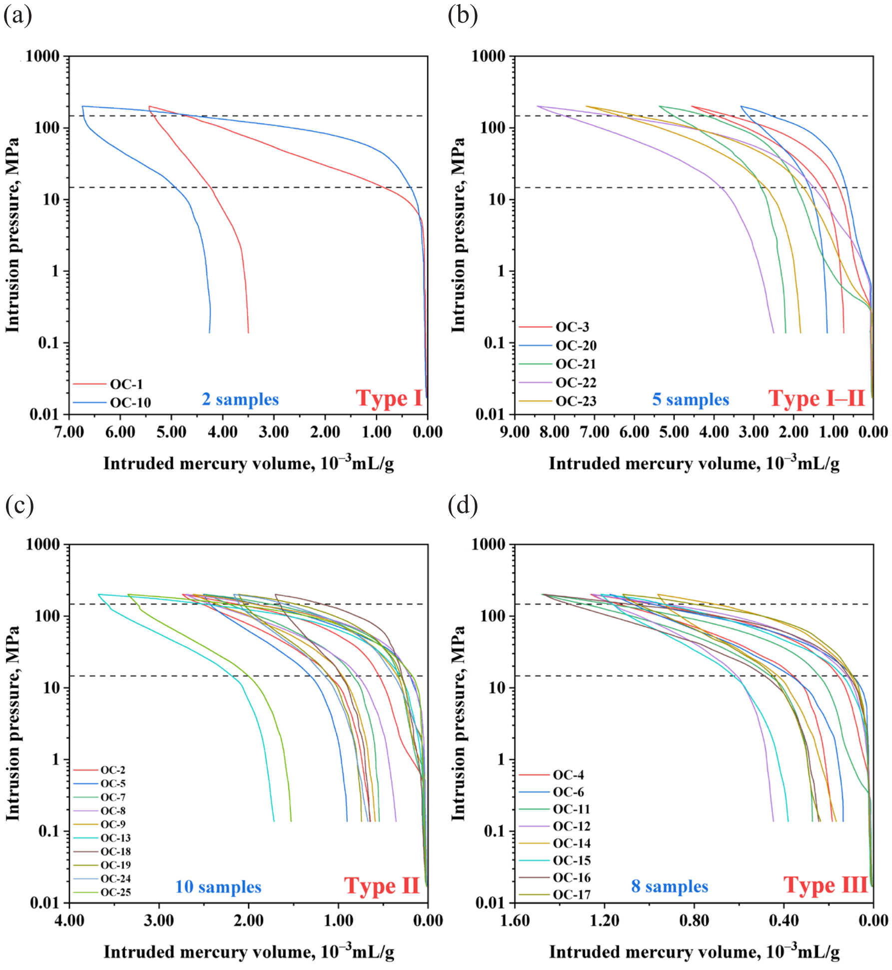

Fig. 7. Classification of mercury saturation pressure curves for Chang 7 shale.

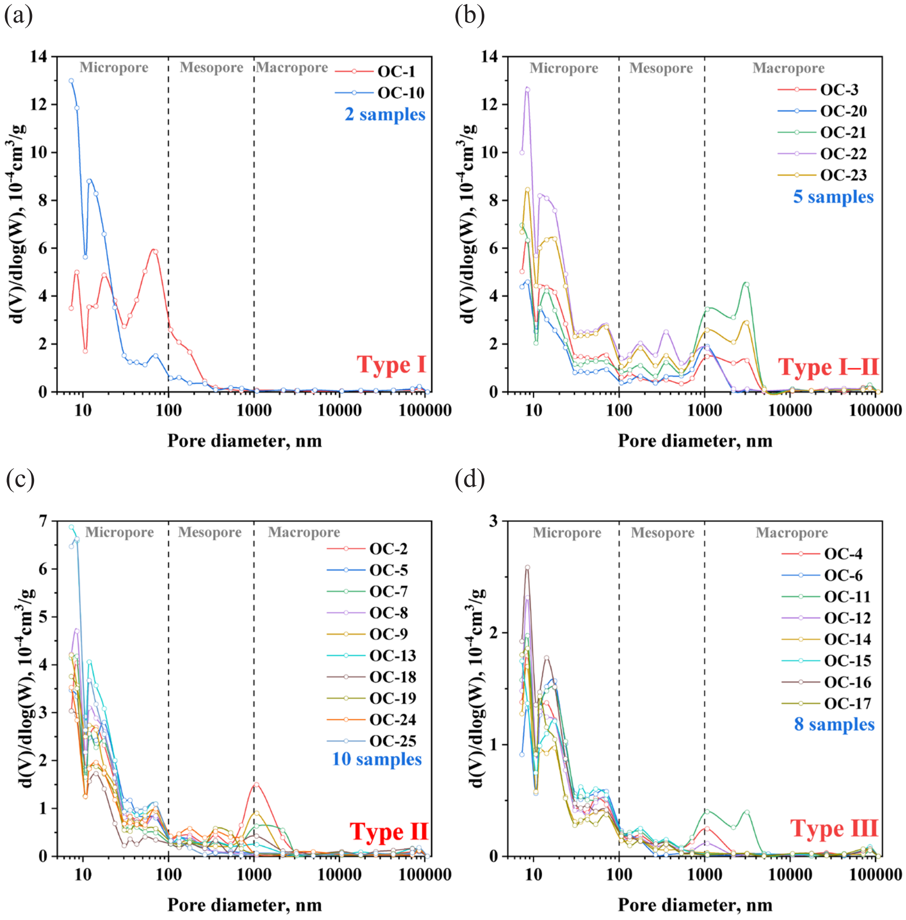

Fig. 8. Pore size distribution of different types of Chang 7 shale based on mercury injection capillary pressure.

The PVs of all samples ranges from 0.0025 to 0.0139 cm^3/g, with an average of 0.0061 cm^3/g. The APDs ranges from 15.29 to 644.58 nm, with an average of 129.26 nm. The average volume fractions of micropores, mesopores, and macropores are 86.65%, 8.38%, and 4.97%, respectively. The average PVs of the four sample types follow the order type I > type I–II > type II > type III (0.0108, 0.0100, 0.0056, and 0.0030 cm^3/g, respectively). The average APDs follow the same order: type I > type I–II > type II > type III (236.71, 215.44, 89.84, and 63.12 nm, respectively).

4.2.3. NMR T_2 *spectrum*

The T_2 spectrum distribution of all samples can be classified into three types: bimodal, trimodal, and bimodal–trimodal transitional (Fig. 9). The first peak (P1) is consistently distributed around 0.5 ms, while the positions of P2 and P3 vary depending on the sample. The bimodal type includes 13 samples, where P2 and P3 merge into a single peak, indicating the presence of two pore scales in the samples. The trimodal type includes five samples, where P2 and P3 significantly develop between 10–1000 ms, indicating that the samples develop at least three pore scales. The bimodal–trimodal transitional type includes seven samples, where the separation between P2 and P3 is not distinct, indicating that the larger-scale pores in these samples are relatively continuous with less distinct spacing.

By comparing the T_2 spectrum distribution of all samples with the PSD based on NA and MICP, it can be observed that the stable P1 in the T_2 spectrum corresponds well to the micropores identified by NA, while P2 and P3 in the T_2 spectrum correspond to the mesopores and macropores in the MICP-based PSD. The key difference is that the T_2 spectrum represents the PSD of all pore spaces within the shale, whereas MICP represents only the pore-throat diameter distribution of the connected parts in the mesopores and macropores.

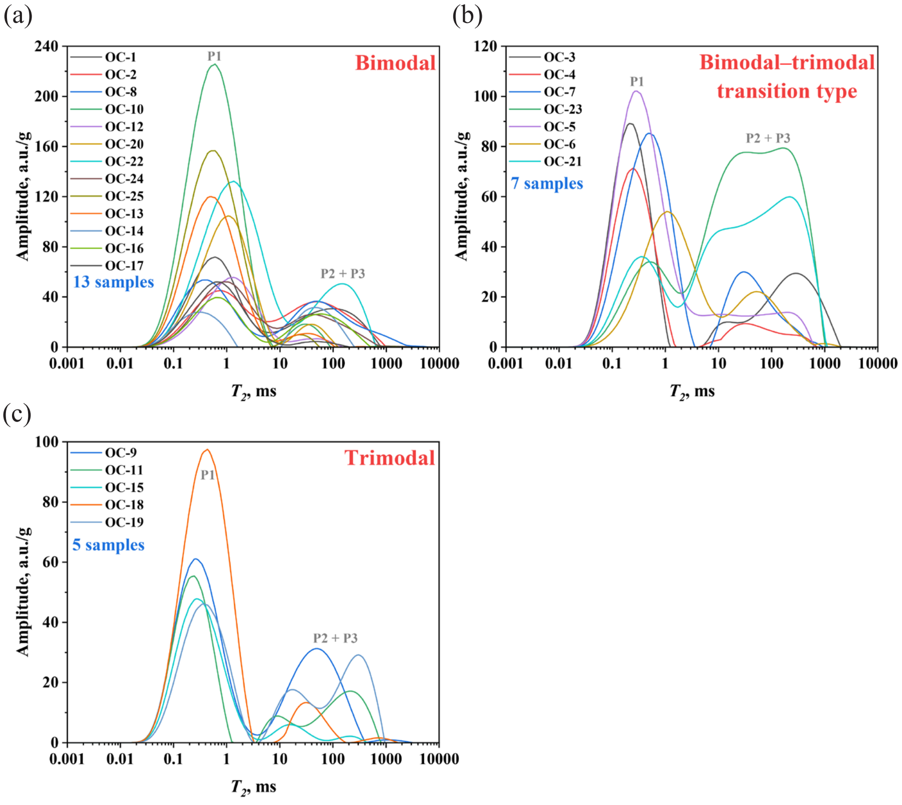

Fig. 9. Classification of NMR T_2 spectrum distribution for Chang 7 shale.

4.3. Distribution of NMR T_2 and T_1–T_2 spectra in different states of shale

The T_2 spectrum and T_1–T_2 spectrum distributions of Ch-7 shale in its original, dry, C_{12}-saturated, and water-saturated states can effectively reveal the relaxation characteristics of different hydrogen nuclei components. The T_2 spectra of all samples in their original state exhibit a prominent left peak and a weak right peak, which correspond to structural water (adsorbed water in the clay matrix) and residual oil or water relaxation signals, respectively (Fig. 10). The original state T_1–T_2 spectrum shows a significant structural water peak around $T_2 = 0.1$ ms and weak residual oil peaks around $T_2 = 0.5$ ms and 2 ms (Fig. 11). The residual oil signals are mainly distinguished into adsorbed and free states by $T_2 = 1$ ms. The T_1 values are distributed in bands, with solid (or semi-solid) kerogen located in the region where T_1–$T_2 > 100$, residual oil signals in the region where T_1–T_2 is between 10–100, and water signals in the region where T_1–$T_2 < 10$, which is consistent with previous studies [14].

In the dry state, the left peak of the shale T_2 spectrum is significantly weakened, while the right peak is slightly reduced. In the T_1–T_2 spectrum, the structural water signal at $T_2 = 0.1$ ms is significantly weakened, but the kerogen and oil signals do not show significant reduction (Figs 10 and 11).

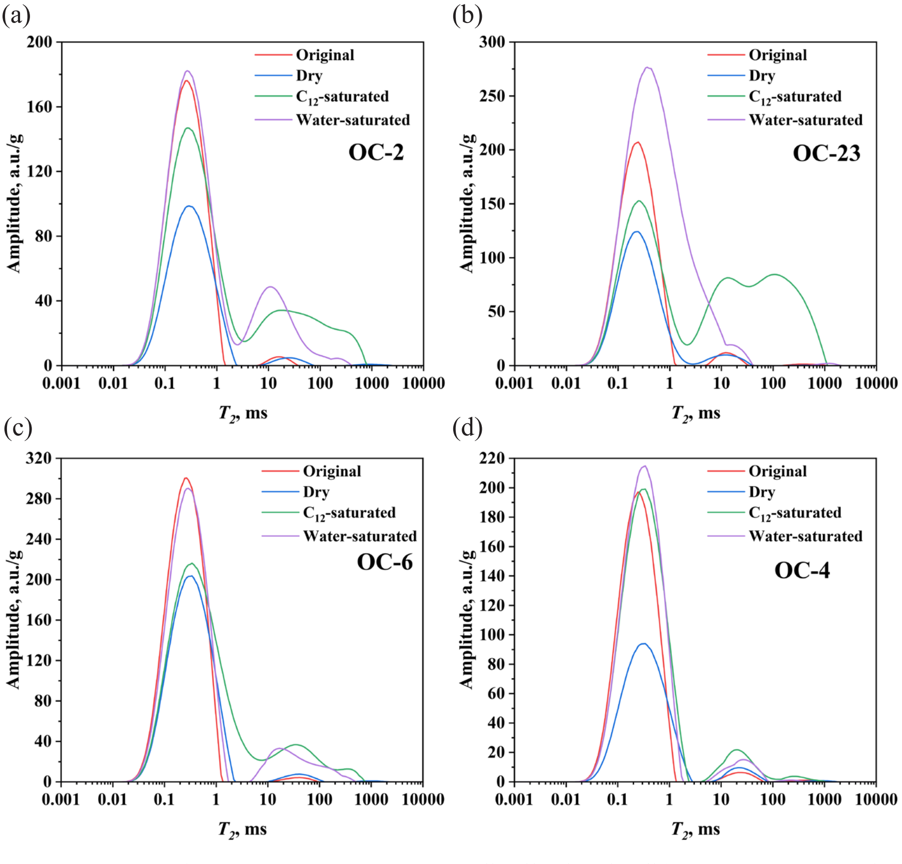

Fig. 10. Comparison of NMR T_2 spectrum distribution in different states of typical Chang 7 shale.

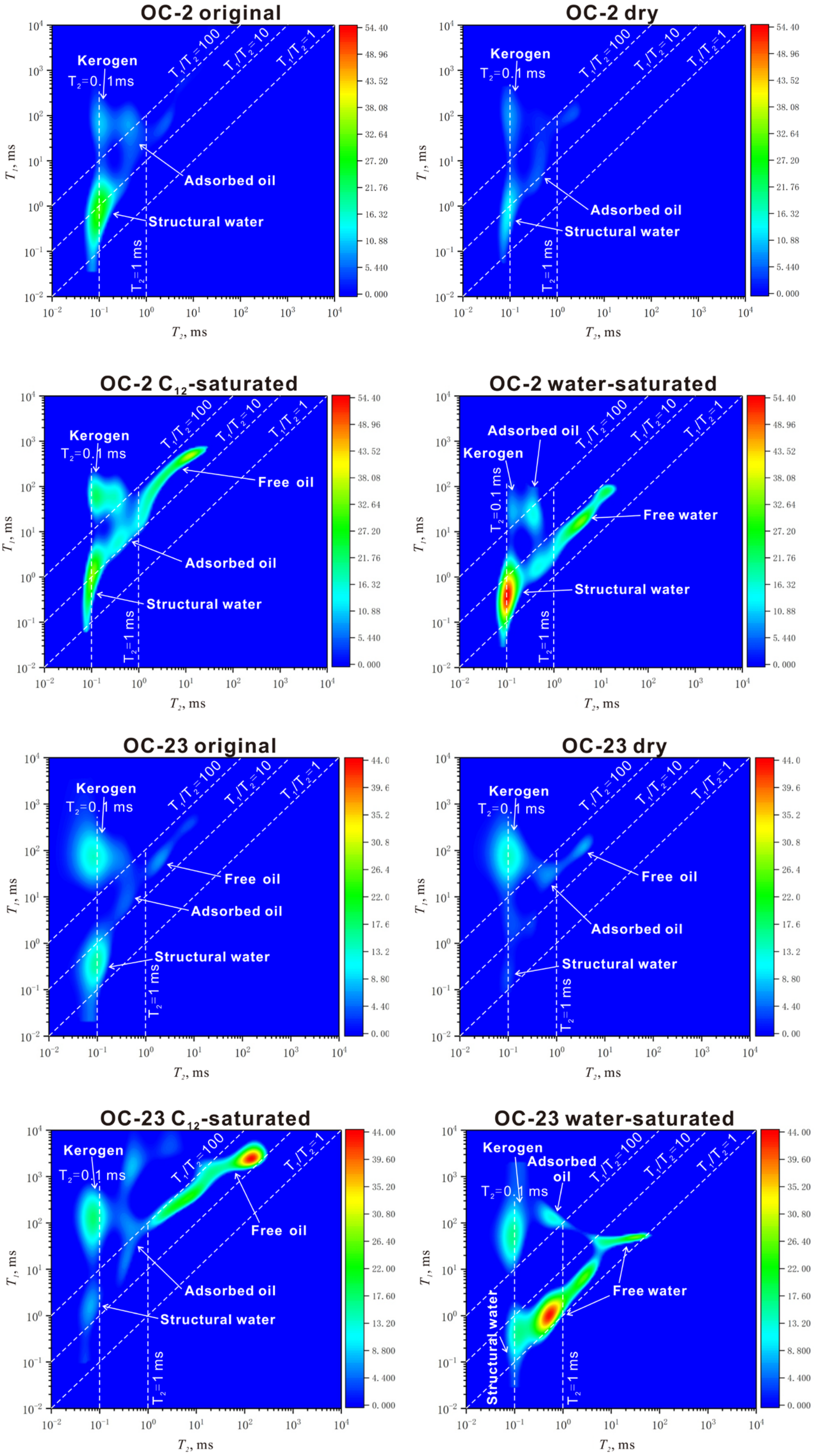

Fig. 11. Comparison of NMR T_1–T_2 spectrum distribution in different states of typical Chang 7 shale.

In the C_{12}-saturated state, the right peak of the T_2 spectrum increases significantly, and the characteristics of the P2 and P3 are apparent, indicating that adsorbed and free oil primarily exist in relatively larger pore spaces (Fig. 10). The signal in the T_1–T_2 spectrum, where T_1/T_2 is between 10–100, increases significantly, and the adsorbed and free states are clearly distinguished by $T_2 = 1$ ms (Fig. 11).

In the water-saturated state, the right peak of the T_2 spectrum shifts slightly to the left compared to the C_{12}-saturated state, especially for samples with low clay mineral content (e.g., OC-23) (Fig. 10). In the T_1–T_2 spectrum, the signal in the region, where T_1/T_2 is between 1–10, increases significantly (Fig. 11). For samples with low clay mineral content (such as OC-23), the water signal peak deviates more toward larger-scale pores compared to the kerogen T_2 signal (Fig. 11b).

4.4. Conversion model of NMR T_2 spectrum to pore size distribution

Due to the uncalibrated PSD in the NMR T_2 spectrum, it is necessary to combine NMR with other quantitative characterization methods to effectively characterize the nano- to microlevel PSD in shale [37]. The pore size conversion model and the calibrated PSD are two key factors determining the accuracy of T_2 pore size analysis. Two types of conversion models, linear and nonlinear, are widely used for calibrating the T_2 spectrum [13]. From the comparison of PSDs obtained through the different methods of NA, MICP, and NMR, it can be seen that the micropores characterized by NA have a good correspondence with the P1 of the T_2 spectrum, while the mesopores and macropores characterized by MICP correspond to the P2 + P3 of the T_2 spectrum in terms of pore scale. This is evident in the pore size merging curve and the T_2 spectrum distribution comparison (Fig. 12). Therefore, this study attempts to establish the pore size conversion model for the T_2 spectrum by fitting the micropores with the PSD based on NA and P1 of the T_2 spectrum, and by fitting the mesopores and macropores with the PSD based on MICP and P2 + P3 of the T_2 spectrum. The fitting equations for the linear model are as follows:

$$\frac{1}{T_2} = \rho_2 \frac{S}{V} = \rho_2 \frac{F_s}{d}, \tag{1}$$

$$d = F_s \rho_2 T_2 = C \times T_2. \tag{2}$$

The fitting equations for the power function model are as follows:

$$\frac{1}{T_2} = \rho_2 \frac{S}{V} = \rho_{2,0} d^m \frac{F_s}{d^n} = \rho_{2,0} F_s d^{m-n}, \tag{3}$$

$$d = \left(F_s \rho_{2,0} T_2\right)^{\frac{1}{n-m}} = \left(F_s \rho_{2,0} T_2\right)^k = C_k T_2^k, \tag{4}$$

where F_s is the pore shape factor, with values of 2, 4, and 6 for plate-like, cylindrical, and spherical pores, respectively, determined based on the shape of the NA adsorption–desorption hysteresis loop; H2, H3, H4, and H2–H3 mixed types have values of 6, 2, 2, and 4, respectively; ρ_2 is the surface relaxation rate, μm/s; $\rho_{2,0}$ is the initial surface relaxation rate, μm/s; and d is the pore diameter, nm.

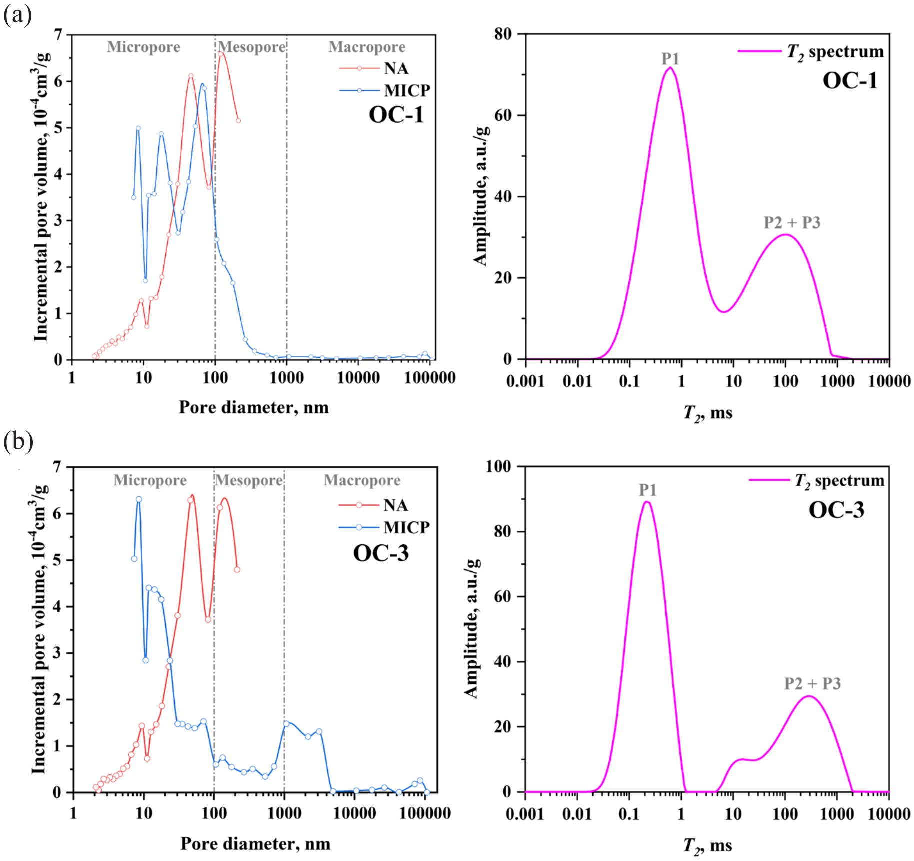

Fig. 12. Comparison of combined pore size distribution based on N_2 adsorption and mercury injection capillary pressure with NMR T_2 spectrum distribution for typical Chang 7 shale.

The specific calibration process can be divided into four steps (Fig. 13a, b):

1. Construct the cumulative PSD and amplitude curve based on NA and the T_2 spectrum P1.
2. Use polynomial fitting on the cumulative amplitude curve of P1 of the T_2 spectrum, obtain the polynomial equation, and calculate the T_2 relaxation times corresponding to the NA data points at the same cumulative frequency.

3. Use the methods described in steps 1 and 2 to obtain the T_2 relaxation times corresponding to P2 + P3 for mesopores and macropores from MICP at the same cumulative frequency.
4. Use linear and power function models to calibrate the T_2 relaxation time and the corresponding pore size, and establish the pore size conversion model.

From the actual calibration results, it is evident that the fitting between the micropore PSD based on NA and the P1 of the T_2 spectrum is quite good, with R^2 generally greater than 0.9 (Fig. 13a). However, the fitting between the mesopore and macropore PSD based on MICP and the P2 + P3 of the T_2 spectrum is poorer, with R^2 values all less than 0.8, indicating a larger error that does not meet the precision requirements of the T_2 spectrum pore size conversion model (Fig. 13b). As mentioned earlier, the PSD based on MICP and the P2 + P3 peaks of the T_2 spectrum differ in their representation of pore space, leading to significant errors in the mesopore and macropore fitting results.

(a)

Nitrogen adsorption – micropore fitting

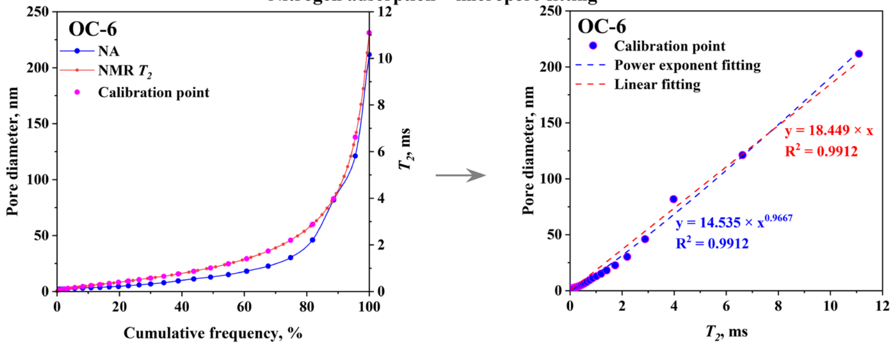

(b)

Mercury injection capillary pressure – meso- and macropore fitting

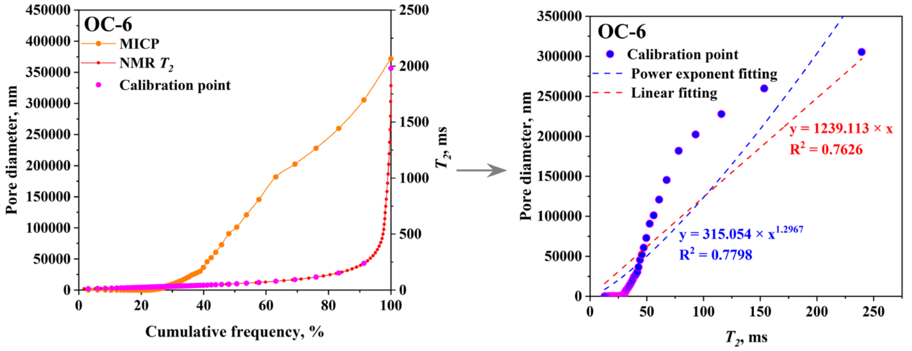

Fig. 13. Schematic of T_2 spectrum calibration and fitting process for typical samples of Chang 7 shale based on nitrogen adsorption- and mercury injection capillary pressure-derived pore size distribution.

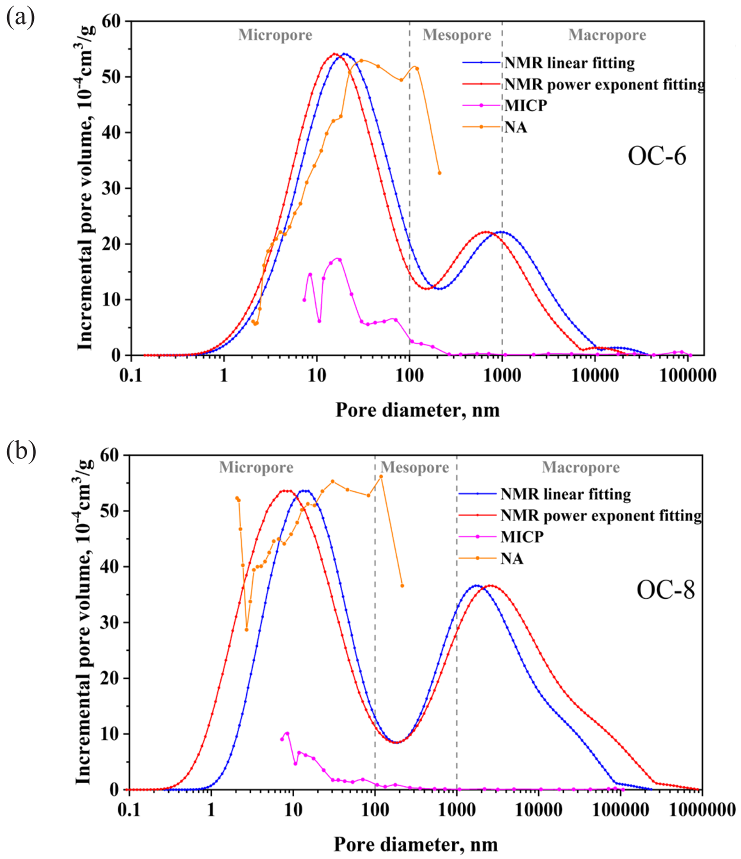

Fig. 14. Comparison of pore size distribution based on N_2 adsorption, mercury injection capillary pressure, and NMR T_2 spectrum derived linear and power exponent fitting for typical Chang 7 shale.

Therefore, despite previous studies attempting to use a combined PSD obtained from NA and MICP to fit the T_2 spectrum and establish a pore size conversion model [37], this study, based on the principle of accuracy, only uses the PSD from NA and the P1 of the T_2 spectrum to calibrate and fit the pore size conversion model.

The specific parameters of the pore size conversion model are listed in Table 3. The average linear model conversion coefficient, C, is 53.591 μm/s, and the average R^2 is 0.9380. For the power function model, the average conversion coefficient, C_k, is 45.825 μm/s, with an average k of 1.1632. The average R^2 is higher, at 0.9612, and the standard deviation is lower, indicating that the power function model provides higher precision for pore size conversion.

The average linear conversion coefficient for 25 samples is calculated, and the power function model is first converted to the linear model before averaging the conversion coefficients. The resulting linear and power function models for pore size conversion in the T_2 spectrum applicable to Ch-7 shale are as follows:

The linear model for pore size conversion from the T_2 spectrum: $d = 53.591 \times T_2$, $R^2 = 0.9380$.

The power function model for pore size conversion from the T_2 spectrum: $\lg(d/45.825) = 1.1632 \times \lg T_2$, $R^2 = 0.9612$.

However, in practical application, since the k value of the power exponential function lacks a clear pore morphology or physical significance, simply averaging all the data may not represent the overall characteristics of the sample. Therefore, the PSD should be calculated based on the average linear conversion model in cases where no definite PSD conversion power exponential function model exists.

By comparing the PSDs from NA, MICP, and the T_2 spectrum, the PV from the T_2 spectrum is normalized using NA-derived PV. The overall PSD from NA shows good consistency with the T_2 spectrum, while the PSD from MICP is consistently lower than that of the T_2 spectrum (Fig. 14). Given that MICP primarily characterizes the connected pore throats, combining MICP with the T_2 spectrum may provide a better method for characterizing the connectivity ratio of pore throats in shale.

Table 3. Characteristic parameters of pore size conversion model for T_2 spectrum of Chang 7 shale samples using linear and power exponential functions

Sample No.	Fs	C	ρ_2	R^2	C_k	k	$\rho_{2,0}$	R^2
OC-1	4	35.466	8.8665	0.9828	30.858	1.1156	5.4073	0.9667
OC-2	2	31.484	15.7420	0.9652	21.557	1.0630	8.9851	0.9778
OC-3	2	162.150	81.0750	0.9325	171.070	1.4666	16.6593	0.9766
OC-4	2	132.960	66.4800	0.9523	136.700	1.4460	14.9964	0.9683
OC-5	4	42.620	10.6550	0.9736	44.247	1.1020	7.7890	0.9513
OC-6	2	18.449	9.2245	0.9912	14.535	0.9667	7.9694	0.9912
OC-7	2	39.345	19.6725	0.8006	16.462	1.4113	3.6386	0.9535
OC-8	2	35.582	17.7910	0.9840	25.227	1.1875	7.5768	0.9905
OC-9	2	58.786	29.3930	0.9531	63.568	1.3397	11.0910	0.8761
OC-10	6	26.356	4.3927	0.9651	16.210	1.0885	2.1541	0.9720
OC-11	2	148.540	74.2700	0.9126	155.200	1.5619	12.6380	0.9730

Table 3. (continued)

Sample No.	Fs	C	ρ_2	R^2	C_k	k	$\rho_{2,0}$	R^2
OC-12	2	15.200	7.6000	0.9760	12.576	1.0232	5.9372	0.9669
OC-13	6	25.205	4.2008	0.9782	19.438	1.0334	2.9434	0.9718
OC-14	4	112.840	28.2100	0.9315	80.554	1.1922	9.9252	0.9785
OC-15	2	54.706	27.3530	0.9424	55.354	1.1323	17.3159	0.9005
OC-16	2	38.154	19.0770	0.9836	29.802	1.0241	13.7570	0.9806
OC-17	2	16.624	8.3120	0.8802	27.684	0.9631	15.7201	0.8831
OC-18	6	55.432	9.2387	0.9047	31.015	1.1930	2.9656	0.9692
OC-19	6	57.397	9.5662	0.9109	32.882	1.2188	2.9274	0.9724
OC-20	6	19.098	3.1830	0.9536	10.760	1.1008	1.4427	0.9758
OC-21	2	76.595	38.2975	0.8136	45.247	1.3643	8.1748	0.9305
OC-22	4	12.970	3.2425	0.9426	22.826	0.7796	13.8169	0.9794
OC-23	2	71.854	35.9270	0.8620	42.931	1.2937	9.1425	0.9519
OC-24	4	23.554	5.8885	0.9960	21.835	0.9402	6.6415	0.9934
OC-25	6	28.415	4.7358	0.9608	17.089	1.0715	2.3567	0.9796
Average value		53.591	21.6958	0.9380	45.825	1.1632	8.4789	0.9612
Standard deviation		41.58	21.83	0.05	43.55	0.18	4.84	0.03

4.5. NMR T_1–T_2 spectrum identification map of shale oil occurrence

The T_1–T_2 spectrum is an effective method for indicating the relaxation characteristics of different types of hydrogen nuclei. In this study, a T_1–T_2 identification map for the Ch-7 shale oil reservoir was developed based on the T_1–T_2 spectral framework established by Fleury and Romero-Sarmiento for gas shale [38] (Fig. 15). This framework identifies six types of shale hydrogen nuclei:

1. Free oil: The T_1–T_2 of free oil displays a linear distribution, located along a line where T_1–T_2 ranges between 10 and 100. The T_2 relaxation time is distributed between 2 ms and the free relaxation time.

2. Adsorbed oil: A typical characteristic of adsorbed oil is the significant range of T_1 relaxation times, with the T_2 distribution mainly between 0.3–0.4 ms.
3. Structural water: The T_1–T_2 of structural water shows a linear distribution along a parallel line where T_1–T_2 ranges from 1 to 10.
4. Free water: In shales with a high clay mineral content, the signal is prominent, centered at $T_2 \approx 0.1$ ms and T_1–$T_2 \approx 5$.
5. Adsorbed water: The relaxation characteristics of adsorbed water are similar to those of free water, but with a larger T_2 peak, approximately 0.2 ms.
6. Kerogen: The T_1–T_2 ratio of kerogen is related to the maturity of organic matter, with the ratio increasing as maturity increases. The T_2 peak is relatively small, around 0.1 ms.

The results of this study provide valuable insights for the development of low-permeability shale reservoirs, particularly highlighting the complex and heterogeneous pore structures observed in the Ch-7 shale, which present challenges for hydrocarbon extraction in formations where fluid migration is restricted. By integrating NMR, MICP, and NA data, the study effectively characterizes pore connectivity and fluid distribution, which are crucial for reservoir assessment. Understanding fine-scale pore structures is essential for optimizing hydraulic fracturing techniques and improving recovery efficiency. The T_2 spectra and developed pore size distribution models can guide the selection of appropriate fracturing methods to enhance hydrocarbon

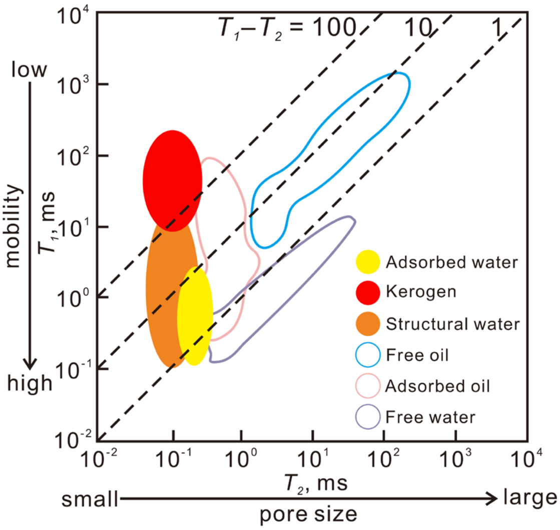

Fig. 15. Identification map of hydrogen nuclear NMR T_1–T_2 spectrum for Chang 7 shale.

recovery. Additionally, the pore characterization models developed here can be applied to similar shale formations globally, offering broader implications for the exploration and exploitation of shale oil and gas resources.

5. Conclusions

1. The Chang 7 shale is thermally mature and mainly composed of organic-rich and organic-bearing argillaceous lithofacies.
2. Based on the nitrogen adsorption (NA) hysteresis loop, the shale can be classified into four types: H2, H3, H4, and H2–H3 mixed type, with type H2 showing the best physical properties. According to the mercury saturation curve, the shale is categorized into four levels of properties, ranging from good to poor. The T_2 spectra were divided into three types: bimodal, trimodal, and bimodal–trimodal transitional.
3. Through segmentation and fitting of NA-derived micropores and mercury injection capillary pressure (MICP)-derived mesopores and macropores with the T_2 spectra, it was found that NA fitting exhibited strong correlation, while MICP was more suitable for evaluating pore throat connectivity in combination with the T_2 spectra.
4. This study developed linear and power-law pore size conversion models for the T_2 spectra of Chang 7 shale, with the power-law model demonstrating higher conversion accuracy. By comparing T_1–T_2 spectra under four conditions – original, dry, C_{12}-saturated, and water-saturated –, the occurrence region characteristics of six hydrogen nucleus components were identified, and a corresponding identification map was established for Chang 7 shale.
5. The findings of this study enhance the understanding of pore structure and hydrocarbon occurrence in low-permeability shale reservoirs, providing valuable insights for optimizing exploration and extraction strategies in such formations.

Data availability statement

The authors confirm that the data supporting the findings of this study are available within the article.

Acknowledgments

This study was jointly supported by the Natural Science Basic Research Program of Shaanxi (grant No. 2024JC-YBQN-0278), the Open Project of National Engineering Laboratory for Exploration and Development of Low Permeability Oil and Gas Fields (grant No. 2023-9901), the National Major Science and Technology Special Project (grant No. 2011ZX05044), and Sinopec Technology Research and Development (grant No. P14150). The publication costs of this article were partially covered by the Estonian Academy of Sciences.

References

1. Montgomery, S. L., Jarvie, D. M., Bowker, K. A., Pollastro, R. M. Mississippian Barnett Shale, Fort Worth basin, north-central texas: gas-shale play with multi-trillion cubic foot potential. *AAPG Bull.*, 2005, **89**(2), 155–175. https://doi.org/10.1306/09170404042
2. Zou, C. N., Zhai, G. M., Zhang, G. Y., Wang, H. J., Zhang, G. S., Li, J. Z. et al. Formation, distribution, potential and prediction of global conventional and unconventional hydrocarbon resources. *Pet. Exp. Dev.*, 2015, **42**(1), 14–28. https://doi.org/10.1016/s1876-3804(15)60002-7
3. Ma, Y. S., Cai, X. Y., Zhao, P. R. China's shale gas exploration and development: understanding and practice. *Pet. Explor. Dev.*, 2018, **45**(4), 589–603. https://doi.org/10.1016/s1876-3804(18)30065-x
4. Mousa, D. A., Abuhagaza, A. A., Mahdi, A. Q., Gentzis, T., Makled, W. A. Assessment of the hydrocarbon potential in the black shales of the Jurassic Khatatba Formation and generated hydrocarbons, North Western Desert, Egypt: depositional mechanism of organic rich rocks related to syn-rift differential subsidence. *Mar. Pet. Geol.*, 2024, **167**, 106975. https://doi.org/10.1016/j.marpetgeo.2024.106975
5. Tan, M. J., Mao, K. Y., Song, X. D., Yang, X., Xu, J. J. NMR petrophysical interpretation method of gas shale based on core NMR experiment. *J. Pet. Sci. Eng.*, 2015, **136**, 100–111. https://doi.org/10.1016/j.petrol.2015.11.007
6. Li, J. B., Lu, S. F., Chen, G. H., Wang, M., Tian, S. S., Guo, Z. Q. A new method for measuring shale porosity with low-field nuclear magnetic resonance considering non-fluid signals. *Mar. Pet. Geol.*, 2019, **102**, 535–543. https://doi.org/10.1016/j.marpetgeo.2019.01.013
7. Liu, J. L., Xie, R. H., Guo, J. F. Numerical investigation of T_2*-based and T_2-based petrophysical parameters frequency-dependent in shale oil. *Energy*, 2024, **313**, 133788. https://doi.org/10.1016/j.energy.2024.133788
8. Zamiri, M. S., Guo, J. F., Marica, F., Romero-Zerón, L., Balcom, B. J. Characterization of kerogen in shale core plugs using T_2*-based magnetic resonance methods. *Fuel*, 2022, **324**(A), 124573. https://doi.org/10.1016/j.fuel.2022.124573
9. Fajt, M., Mazur-Rosmus, W., Stefańska, A., Kochman, A., Krzyżak, A. T. Chert outcrops differentiation by means of low-field NMR relaxometry. *Sci. Rep.*, 2024, **14**(1), 25280. https://doi.org/10.1038/s41598-024-75945-6
10. Shelyapina, M. G. NMR relaxation to probe zeolites: mobility of adsorbed molecules, surface acidity, pore size distribution and connectivity. *Molecules*, 2024, **29**(22), 5432. https://doi.org/10.3390/molecules29225432
11. Liu, Y., Yao, Y. B., Liu, D. M., Zheng, S. J., Sun, G. X., Chang, Y. H. Shale

pore size classification: an NMR fluid typing method. *Mar. Pet. Geol.*, 2018, **96**, 591–601. https://doi.org/10.1016/j.marpetgeo.2018.05.014

12. Maxey, D., Afari, S., Jabbari, H. NMR relaxometry insights into pore-level sweep efficiency for methane infusion IOR in unconventional reservoirs. *Geoenergy Sci. Eng.*, 2025, **245**, 213527. https://doi.org/10.1016/j.geoen.2024.213527
13. Zhang, P. F., Lu, S. F., Li, J. Q. Characterization of pore size distributions of shale oil reservoirs: a case study from Dongying sag, Bohai Bay basin, China. *Mar. Pet. Geol.*, 2019, **100**, 297–308. https://doi.org/10.1016/j.marpetgeo.2018.11.024
14. Zhang, P. F., Lu, S. F., Li, J. Q. Characterization of pore size distributions of shale oil reservoirs: a case study from Dongying sag, Bohai Bay basin, China. *Mar. Pet. Geol.*, 2019, **100**, 297–308. https://doi.org/10.1016/j.marpetgeo.2018.11.024
15. Liu, K. Q., Zhang, Z. C., Ostadhassan, M. The application of Gaussian distribution deconvolution method to separate the overlapping signals in the 2D NMR map. *Pet. Sci.*, 2023, **20**(3), 1513–1520. https://doi.org/10.1016/j.petsci.2022.11.006
16. Silletta, E. V., Delfa, G. M., Velasco, M. I., Donadelli, J. A., Monti, G. A., Smal, C. et al. Quantification of imbibed heptane in shale rocks determined by edited T_1–T_2 nuclear magnetic resonance relaxation experiments at high magnetic field. *Energy Fuels*, 2022, **36**(18), 10794–10802. https://doi.org/10.1021/acs.energyfuels.2c01554
17. Bratland, A. M. L., Pavlin, T., Djurhuus, K., Seland, J. G. Characterising oil and water in porous media using correlations between internal magnetic gradient and transverse relaxation time. *J. Magn. Reson.*, 2020, **310**, 106649. https://doi.org/10.1016/j.jmr.2019.106649
18. Zhou, Y. Q., You, L. Z., Zi, H., Lan, Y. Y., Cui, Y. L., Xu, J. F. et al. Determination of pore size distribution in tight gas sandstones based on Bayesian regularization neural network with MICP, NMR and petrophysical logs. *J. Nat. Gas Sci. Eng.*, 2022, **100**, 104468. https://doi.org/10.1016/j.jngse.2022.104468
19. Fajt, M., Fheed, A., Machowski, G., Sowiżdżał, A., Krzyżak, A. T. Modified low-field NMR method for improved pore space analysis in tight Fe-bearing siliciclastic and extrusive rocks. *Lithosphere*, 2024, **3**, 157. https://doi.org/10.2113/2024/lithosphere_2024_157
20. Bardenhagen, I., Dreher, W., Fenske, D., Wittstock, A., Bäumer, M. Fluid distribution and pore wettability of monolithic carbon xerogels measured by ^{1}H NMR relaxation. *Carbon*, 2014, **68**, 542–552. https://doi.org/10.1016/j.carbon.2013.11.033
21. Wang, Y., Cheng, H. F., Hu, Q. H., Liu, L. F., Jia, L. B., Gao, S. S. et al. Pore structure heterogeneity of Wufeng-Longmaxi shale, Sichuan Basin, China: evidence from gas physisorption and multifractal geometries. *J. Pet. Sci. Eng.*, 2022, **208**(A), 109313. https://doi.org/10.1016/j.petrol.2021.109313
22. AlKharraa, H., Wolf, K.-H., AlQuraishi, A., Al Abdrabalnabi, R., Mahmoud, M., Zitha, P. Microscopic CO_2 injection in tight rocks: implications for enhanced oil recovery and carbon geo-storage. *Energy Fuels* 2023, **37**(23), 19039–19052. https://doi.org/10.1021/acs.energyfuels.3c03403

23. Li, J. B., Jiang, C. Q., Wang, M., Lu, S. F., Chen, Z. H., Chen, G. H. et al. Adsorbed and free hydrocarbons in unconventional shale reservoir: a new insight from NMR T_1–T_2 maps. *Mar. Pet. Geol.*, 2020, **116**, 104311. https://doi.org/10.1016/j.marpetgeo.2020.104311
24. Guo, R. L., Li, S. X., Zhou, X. P., Guo, Q. H., Li, S. T., Chen, J. L. et al. Multi-isothermal stage pyrolysis of the Chang 7_3 shale oil reservoirs, Ordos Basin: implications for oil occurrence states and in situ conversion exploitation. *A ACS Earth Space Chem.*, 2022, **6**(4), 1143–1162. https://doi.org/10.1021/acsearthspacechem.2c00057
25. Guo, R. L., Yu, G. M., Wen, K. F., Liu, F., Zhao, J. Z., Bai, Y. B. et al. Pore characteristics and its impact on shale oil occurrence of lacustrine shale from Chang 7, Ordos Basin. *Pet. Sci. Technol.*, 2024, 1–20. https://doi.org/10.1080/10916466.2024.2391481
26. Wang, Y., Liu, L. F., Cheng, H. F. Pore structure of Triassic Yanchang mudstone, Ordos Basin: insights into the impact of solvent extraction on porosity in lacustrine mudstone within the oil window. *J. Pet. Sci. Eng.*, 2020, **195**, 107944. https://doi.org/10.1016/j.petrol.2020.107944
27. Yang, Y., Li, W., Ma, L. Tectonic and stratigraphic controls of hydrocarbon systems in the Ordos basin: a multicycle cratonic basin in central China. *AAPG Bull.*, 2005, **89**(2), 255–269. https://doi.org/10.1306/10070404027
28. Guo, R., Xie, Q., Qu, X., Chu, M., Li, S., Ma, D. et al. Fractal characteristics of pore-throat structure and permeability estimation of tight sandstone reservoirs: a case study of Chang 7 of the Upper Triassic Yanchang Formation in Longdong area, Ordos Basin, China. *J. Pet. Sci. Eng.*, 2019, **184**, 106555. https://doi.org/10.1016/j.petrol.2019.106555
29. Xie, X. Y. Provenance and sediment dispersal of the Triassic Yanchang Formation, southwest Ordos Basin, China, and its implications. *Sediment. Geol.*, 2016, **335**, 1–16. https://doi.org/10.1016/j.sedgeo.2015.12.016
30. Zhang, P. F., Lu, S. F., Li, J. Q., Xue, H. T., Li, W. H., Zhang, P. Characterization of shale pore system: a case study of Paleogene Xin'gouzui Formation in the Jianghan basin, China. *Mar. Pet. Geol.*, 2019, **100**, 297–308. https://doi.org/10.1016/j.marpetgeo.2018.11.024
31. Zhang, P. F.. Lu, S. F., Li, J. Q., Zhang, J., Xue, H. T., Chen, C. Comparisons of SEM, low-field NMR, and mercury intrusion capillary pressure in characterization of the pore size distribution of lacustrine shale: a case study on the Dongying Depression, Bohai Bay Basin, China. *Energy Fuels*, 2017, **31**(9), 9232–9239. https://doi.org/10.1021/acs.energyfuels.7b01625
32. Mukhopadhyay, P. K., Wade, J. A., Kruge, M. A. Organic facies and maturation of Jurassic/Cretaceous rocks, and possible oil-source rock correlation based on pyrolysis of asphaltenes, Scotian Basin, Canada. *Org. Geochem.*, 1995, **22**(1), 85–104. https://doi.org/10.1016/0146-6380(94)00061-1
33. Zhang, P. F., Yin, Y. J., Lu, S. F., Li, J. Q., Chang, X. C., Zhang, J. J. et al. Insights into pore structures and multifractal characteristics of shale oil reservoirs: a case study from Dongying Sag, Bohai Bay Basin, China. *Energy Fuels*, 2022, **36**(15), 8224–8237. https://doi.org/10.1021/acs.energyfuels.2c01763

34. Wang, L., Li, W., Liu, Q., Wang, D., Zhang, M., Bai, B. Lithofacies characteristics and sedimentary environment of Chang 7 black shale in the Yanchang Formation, Ordos Basin. *J. Palaeogeogr.*, 2023, **25**(3), 598–613.
35. Thommes, M., Kaneko, K., Neimark, A. V., Olivier, J. P., Rodriguez-Reinoso, F., Rouquerol, J. et al. Physisorption of gases, with special reference to the evaluation of surface area and pore size distribution (IUPAC Technical Report). *Pure Appl. Chem.*, 2015, **87**, 9–10. https://dx.doi.org/10.1515/pac-2014-1117
36. Rouquerol, J., Avnir, D., Everett, D. H., Fairbridge, C., Haynes, M., Pernicone, N. et al. Guidelines for the characterization of porous solids. In: *Characterization of Porous Solids III* (Rodríguez-Reinoso, F., Rouquerol, J., Unger, K. K., Sing, K., eds). Elsevier, 1994, 1–9.
37. Yan, P. Y., Guo, J. F., Marica, F., Balcom, B. J. Pore size distribution measurement with magnetic resonance T_2 distributions outside the fast diffusion regime. *Geoenergy Sci. Eng.*, 2023, **230**, 212226. https://doi.org/10.1016/j.geoen.2023.212226
38. Fleury, M., Romero-Sarmiento, M. Characterization of shales using T_1–T_2 NMR maps. *J. Pet. Sci. Eng.*, 2016, **137**, 55–62. https://doi.org/10.1016/j.petrol.2015.11.006